14th International Symposium on Turbulence and Shear Flow Phenomena (TSFP14)
Heidelberg, Germany, July 28–31, 2026

SPARSE-SENSOR INSTANTANEOUS FLOW RECONSTRUCTION AROUND A THICK AIRFOIL NEAR STALL UNDER DIFFERENT TURBULENT INFLOW CONDITIONS

Quentin Bucquet
EM2C, CentraleSupélec
Université Paris-Saclay
France
quentin.bucquet@centralesupelec.fr

Bérengère Podvin
EM2C, CentraleSupélec
Université Paris-Saclay
France

Caroline Braud
LHEEA, CNRS
Centrale Nantes, Nantes Université
France

Emmanuel Guilmineau
LHEEA, CNRS
Centrale Nantes, Nantes Université
France

Salvatore Iavarone
EM2C, CentraleSupélec
Université Paris-Saclay
France

ABSTRACT

Wind turbines operate in a unsteady turbulent atmospheric environment, which conditions their performance. However, estimating unsteady aerodynamic loads is particularly difficult in operating conditions, as only limited surface information is typically available. As a first step to address this challenge, we present an approach that reconstructs the instantaneous flow around a thick airfoil from sparse pressure sensor data. The model combines Proper Orthogonal Decomposition (POD) and shallow neural networks and is trained on a 2D Unsteady Reynolds-Averaged Navier-Stokes (URANS) database with three different freestream intensity levels. We show that the model is able to reconstruct the instantaneous field with less than 5% error with 7 pressure sensors, opening promising perspectives for experimental applications.

INTRODUCTION

Wind turbines operate in the unsteady environment of the atmospheric boundary layer, which is characterized by the presence of turbulence, extreme events (gusts), as well as shear, rotation, and stratification effects (Porté-Agel, 2020). These conditions impact the onset of stall and affect the aerodynamic performance of the airfoil. One important parameter is the freestream turbulence level, which was examined in an early study by Stack (1931), who considered five different airfoils and found that high turbulence intensities delayed the onset of stall and led to a higher lift coefficient at chord-based Reynolds numbers larger than 10^5. These observations were generally confirmed by later investigations, albeit some variations were observed for different airfoils : Devinant (2002) predicted a higher stall angle and higher maximum lift for a NACA 654-421 airfoil, while Maldonado (2015) reported an improvement of the aerodynamic performance for a NREL S809, but did not observe a change in the stall angle. A review of the effect of turbulence on the stall angle, maximum lift coefficient and lift slope, can be found in Li & Hearst (2021).

The influence of turbulence on the wake dynamics has also been the object of both experimental and numerical studies. Gambuzza & Ganapathisubramani (2023) showed that the wake behind a wind turbine airfoil evolved more rapidly for high turbulence intensity and low integral time scale flows. Vahidi & Porté-Agel (2024) used Large Eddy Simulation (LES) to study the effect of turbulent upstream scales on the development of the wake behind a wind turbine. They found that large inflow scales led to more wake meandering in the lateral and vertical directions, and were also associated with a faster wake recovery. The numerical LES investigation performed by Hodgson *et al.* (2023) considering the interaction between wake recovery of a single turbine and the turbulent inflow highlighted the importance of accounting for inflow turbulent time scales in addition to the turbulence intensity, as enhanced wake recovery is reached for short inflow time scales.

It should be noted that numerical modeling of a wind turbine in real-life conditions at high Reynolds numbers (larger than 10^6) still remains a challenge for high-fidelity LES, due to its large computational requirements. In this context, the URANS approach appears to offer a good trade-off between accuracy and computing cost. Sheidani *et al.* (2023) compared URANS and LES approaches to predict the flow behind a vertical axis wind turbine. They concluded that, although LES provided a more detailed description, the main features of the wake region were correctly recovered by URANS. Pagamonci *et al.* (2025) studied the dynamics of a floating offshore wind turbine and found that URANS represented a viable option to determine the impact of realistic turbulence.

It is therefore essential to get access to the inflow conditions, such as the angle of attack (AoA) or turbulent intensity (TI), in order to successfully estimate the aerodynamic loads on the blade and the downstream wake. This information can be evaluated experimentally, but not *in situ*, where only partial measurements (generally from wall pressure sensors) are available. It is therefore necessary to build a reliable estimator that can perform the nonlinear mapping between sparse pressure signals and full-order velocity fields.

Thus, the objective of this work is the instantaneous reconstruction of the velocity field around a thick airfoil using a single-time set of wall pressure measurements for turbulent inflows. In the absence of freestream turbulence, good results were obtained with an approach based on a shallow network (Erichson *et al.*, 2020) combined with POD (Bucquet *et al.*, 2025). The challenge here is to determine whether the model is able to predict the influence of the freestream turbulence intensity as well as that of the angle of attack, and to disentangle the effects of these two parameters. In particular, we investigate whether the inflow turbulence characteristics can be inferred from sparse pressure data, and how these inflow properties influence the accuracy of the reconstruction.

DATASET PRESENTATION

The present dataset comprises two-dimensional simulations of a wind turbine airfoil, whose geometry was extracted from the 3D scan of a real operating 2MW wind turbine at 80% of the rotor diameter. The airfoil exhibits a chord length $c = 1.25$ m and a thickness of 20% (Braud *et al.*, 2024).

Simulations are performed using the ISIS-CFD flow solver (Visonneau *et al.*, 2014), developed by Centrale Nantes and CNRS as part of the FINE™/Marine computing suite, and use an incompressible Unsteady Reynolds-Averaged Navier-Stokes (URANS) approach. Turbulence is modeled using the $k-\omega$ SST model. The transport equations are spatially discretized using a finite volume method on an unstructured mesh, which is dynamically refined or coarsened via Adaptive Mesh Refinement (AMR). A constant time step, defined as $\Delta t U_\infty / c = 0.01$ convective time units (where U_∞ is the inlet velocity and c the blade chord), is applied across all simulations. Flow field snapshots are stored every 5 time steps. The Taylor micro-scale λ is used as turbulent length scale to prescribed the desired turbulence intensity levels the inlet boundary condition according to Mishra *et al.* (2024). The chord-based Reynolds number is $\mathrm{Re} = 4.5 \times 10^6$, reproducing full-scale conditions in the CSTB climatic wind tunnel (Neunaber *et al.*, 2022; Braud *et al.*, 2024). A comparison of experimental and numerical global loads, presented in Neunaber *et al.* (2022), demonstrated good agreement.

The dataset includes simulations at three AoA : 14°, 15°, and 16°. These angles were selected to investigate the onset of stall, where the boundary layer starts to detach. These AoA are specifically retained as they maximize the lift of the studied airfoil (see Neunaber *et al.*, 2022) and affect its performance. To replicate the turbulent atmospheric environment experienced by wind turbines, four freestream turbulence intensities ($\mathrm{TI} = \sqrt{\frac{2}{3} k_\infty} / U_\infty$, with k_∞ the inlet turbulent kinetic energy) are considered: 0% (case where no turbulence is added), 0.3%, 3% and 5.5%, corresponding to the four levels studied in Mishra *et al.* (2022). While these levels are slightly lower than those typically observed in the atmospheric boundary layer (typically $5-20\%$ in Kaimal & Finnigan, 1994), they are consistent with values tested in high-Reynolds number experimental flows (1.5% tested in Mishra *et al.*, 2022) and have a measurable impact on stall behavior and wake flow dynamics.

Fig. 1 shows the distribution of the mean pressure coefficient C_p and its standard deviations σ_{C_p} around the airfoil for each AoA and each TI levels. The effect of increasing the AoA is visible on the C_p distribution, where an increase in AoA is correlated with a displacement of the steady separation point (defined as the first point along the chord where the pressure coefficient becomes nearly constant) towards the leading edge. Additionally, increasing the AoA translates in an overall increase in the variance levels on the blade, related to stronger fluctuations specific of stalled flow regimes, while the opposite is observed with turbulence intensity, as shown on the distribution of σ_{C_p}. Interestingly, a local variance maxima is seen at $x/c \approx 0.5$ (close to the steady separation point) for all configurations, except for 14°, TI = 3% and 5.5% which can be be associated with attached flow regimes.

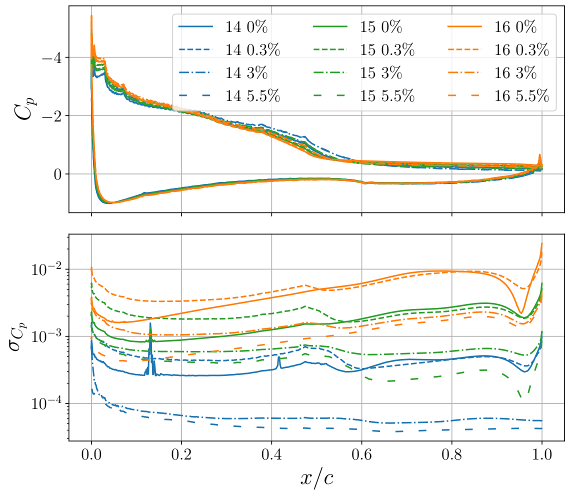

Figure 1: Distributions of the time-averaged pressure coefficient C_p (top) and its standard deviations σ_{C_p} (bottom) around the airfoil.

The flow is therefore affected by the AoA as well as the TI level, in agreement with the literature (Mishra? autres ref?). To characterize the influence of the two parameters and assess the reliability of the reconstruction in more detail, we define additional physics-based metrics for both steady and unsteady flow features.

Time-averaged metrics

The mean flow metrics primarily focus on the wake characteristics. Here, $\bar{\cdot}$ denotes a time-averaged quantity. Three key wake quantities are defined. The **wake width (δ)** corresponds to the spanwise distance at which the time-averaged velocity deficit, $\Delta u(x,y) = (U_\infty - \overline{u}(x,y))$, reaches $\Delta u(x, y = \delta) = \frac{1}{2} \max_y \Delta u(x)$. The **wake deflection angle (α)** is defined as the angle between the line connecting the locations of the maximum velocity deficit and the chord line. It is computed as: $\alpha = \arctan\left(\frac{y_{\max} - y_0}{x_{\max} - x_0}\right)$ where $(x_{\max}, y_{\max})$ are the coordinates of the maximum velocity deficit, and (x_0, y_0) are the coordinates of the trailing edge. Finally, the **maximum transverse gradient** ($\max_y \left| \frac{\partial \overline{u}}{\partial y} \right| (x)$) captures the intensity of shear and turbulent diffusion through turbulent mixing.

Fig. 2 illustrates the streamwise evolution of these three time-averaged wake characteristics. For each feature, a distinction can be made between the near-wake $x/c < 2.5$, where $x/c = 1$ corresponds to the trailing edge location and is strongly influenced by trailing edge effects, and the far-wake $x/c > 2.5$, which is less dependent on trailing edge effects and exhibits consistent asymptotic trends.

In the near-wake region, δ increases with the angle of attack. Higher AoA values result in wider wakes. The influence of flow turbulence on α is primarily observed in the near-wake region. Here, increased turbulence intensity is associated with a smaller peak in α. Conversely, the peak in α increases with AoA. In the far-wake region, only the influence of the AoA remains significant, with higher AoA values corresponding to larger α. The effects of AoA and TI on the maximum transverse gradient are more complex. For a fixed turbulence level, increasing the AoA leads to a larger drop in the near-wake region, indicative of strong turbulent diffusion and effective mixing. However, this trend reverses in the far-wake region, where lower AoA values correspond to lower max $\left|\frac{\partial \overline{u}}{\partial y}\right|$ and thus more significant turbulent mixing, enabling faster wake recovery. A similar effect is observed for TI: low turbulence intensities are associated with stronger mixing in the near-wake, while highly turbulent flows enhance mixing in the far-wake.

Two cases stand out: 14° with TI = 3% and 5.5%. These cases are characterized by narrower wakes and reduced mixing, revealing an attached flow regime. This observation aligns with the findings of Stack (1931), confirming that high turbulence intensities delay the onset of stall. More generally, these three time-averaged quantities clearly allow for a distinction between low TI levels (< 0.3%) and moderate TI levels (> 3%) across all angles of attack.

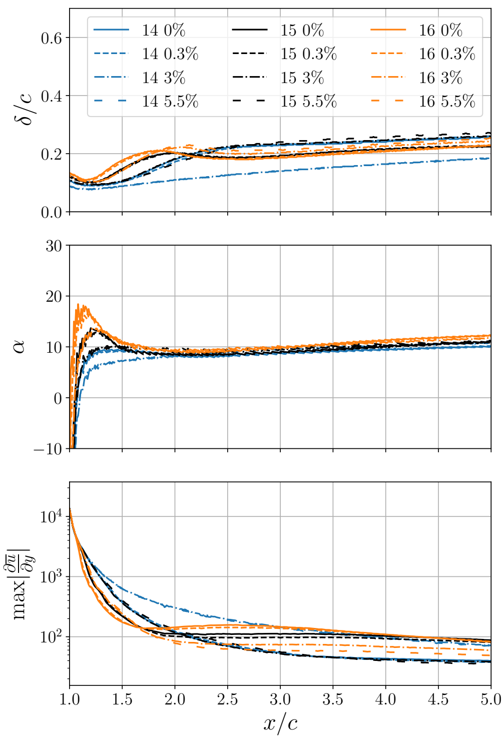

Figure 2: Streamwise evolutions of the wake width δ/c (top), the wake angle deflection α (middle) and the maximum transverse gradient max$\left|\frac{\partial \overline{u}}{\partial y}\right|$ (bottom).

Turbulent metrics

Since the reconstruction method aims to recover instantaneous velocity fields, we now focus on the time-dependent turbulent features of the wake, which are assessed using two turbulent characteristics : the **vertical profiles of the streamwise turbulent intensity** ($T_u = \sqrt{\overline{u'^2}}/U_\infty$), and the **pre-multiplied frequency spectrograms** (fS_u).

The vertical T_u profiles are evaluated at various streamwise locations in the wake, as illustrated in Fig. 3. For all configurations, the profiles are asymmetric and exhibit distinct peaks: one sharp, high-energy peak in the bottom shear layer, and several narrower, lower-energy peaks in the upper shear layer. The position and intensity of the peaks depend on the angle of attack as well as the turbulence intensity (particularly at 16°, with an abrupt change in profiles from 0.3% to 3%).

Spectrograms fS_u are derived from the spectral analysis of the streamwise velocity field and evaluated in a vertical section at $x/c = 2$ in the wake. The spectral content confirms the energy level trends observed in Fig. 3: energy levels increase with AoA, but decrease with TI. Additionally, it can be observed that while increasing the AoA reduces the dominant frequency, increasing TI has the opposite effect, raising the dominant frequency.

These turbulent flow features will serve as metrics for comparing the reconstructed flow state with the simulation results, hereafter referred to as the “ground truth.”

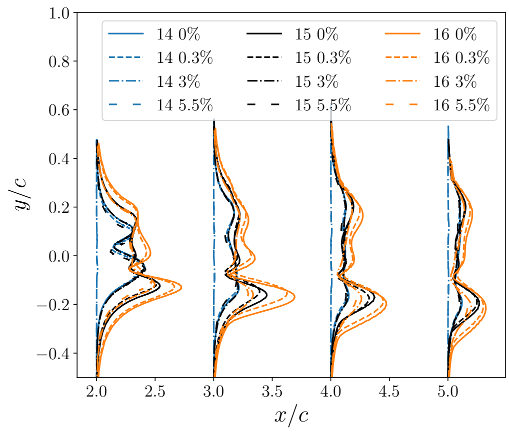

(a)

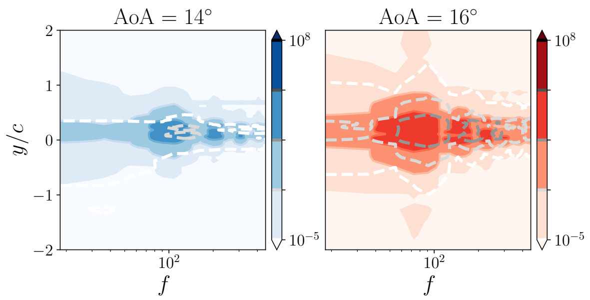

(b)

Figure 3: (a) Vertical profiles of T_u at four streamwise locations (profiles are aligned with respect to the wake center). (b) Spectrograms of the pre-multiplied velocity spectra fS_u in the $x/c = 2$ section at 14° (left) and 16° (right). Blue shaded regions denote the TI= 0% cases, orange contours denote TI= 5.5% cases.

METHODS

This section details the methods used to reconstruct the velocity field from a limited number of wall pressure measurements. We first describe the selection process for the sparse sensor locations, followed by the model used for flow reconstruction.

Sparse sensing method

The sparse sensing approach implemented in the context of this study is a variance-based method denoted as the spatially-clustered maximum variance (SCMV) approach. Thus, it aims to identify the sensors that contribute most significantly to the variance of the pressure coefficient (C_p), while ensuring adequate spatial coverage of the airfoil surface. This spatial constraint is enforced through geometric clustering or partitioning of the surface. To ensure a robust description of the flow dynamics across the full range of AoA and TI, the most relevant sensors are selected for each configuration. A spatial constraint is then applied to prevent sensor clustering and ensure a well-distributed sensor placement.

This approach is detailed in Alg. 1. Considering the trade-off between reconstruction accuracy and number of sensors, an optimal number of $p = 7$ sensors is chosen in this study, given by a sensitivity study detailed in Bucquet *et al.* (2025).

Algorithm 1 SCMV approach

```
Input: Blade pressure field C_p, number of clusters n_c,
  variance threshold σ²_thres, minimum distance d_min
Output: Selected sensor locations
Cluster blade points into n_c clusters based on spatial positions
for each angle of attack AoA_i do
    Compute total variance of C_p in each cluster
    Select the first p_i most energetic clusters
    Choose locations of maximum variance within these p_i clusters
    if selected locations are closer than d_min then
        Move the point with lower variance to enforce distance d_min
    end if
end for
Concatenate all p selected sensors
if concatenated sensors are closer than d_min then
    Keep the point with higher variance and remove the other
end if
```

Reconstruction model: SNN-POD

This section briefly presents the SNN-POD model used for flow field reconstruction. A detailed description of the methodology, architecture, and training strategy is provided in Bucquet *et al.* (2025).

The SNN-POD framework blends POD with the shallow decoder architecture introduced in Erichson *et al.* (2020) to reconstruct the instantaneous streamwise velocity field in the full-order computational domain from a single-time set, spatially sparse pressure measurements, thus avoiding memory requirements. Due to the high dimensionality of the unsteady velocity field (91912 grid points), a linear reduced-order modeling is performed using POD, yielding a low-order latent representation of the flow dynamics.

Given a snapshot matrix of velocity fluctuations $\mathbf{X} \in \mathbb{R}^{N_u \times N_{\text{train}}}$, defined as $u(\mathbf{x}, t_k, \text{AoA}, \text{TI}) = \langle u(\mathbf{x}) \rangle + \mathbf{X}$, where $\langle u(\mathbf{x}) \rangle$ denotes the ensemble-averaged mean flow computed over all training configurations (AoA,TI), the POD decomposition is then $\mathbf{X} = \mathbf{\Phi_u S_u A_u}^{\text{T}}$. Here, $\mathbf{\Phi_u} \in \mathbb{R}^{N_u \times r}$ contains the retained POD spatial modes, $\mathbf{S_u} \in \mathbb{R}^{r \times r}$ is the diagonal matrix of singular values ordered by decreasing magnitude, $\mathbf{A_u} \in \mathbb{R}^{N_{\text{train}} \times r}$ gathers the corresponding temporal coefficients, and r is the number of retained modes.

A shallow neural network (SNN) is then implemented to learn the nonlinear mapping between sparse pressure measurements and the POD latent space. Following Bucquet *et al.* (2025), the POD modes are partitioned into steady and unsteady components, which are reconstructed independently using two distinct shallow neural networks. This separation was shown to significantly improve the reconstruction accuracy of the dominant flow features.

To further prioritize the accurate reconstruction of energetically dominant modes, a singular-value-weighted loss function is introduced during training,

$$\mathscr{L}_{\text{POD}} = \left\| \mathbf{S_u}_\gamma \left(\mathbf{A_u}_\gamma - \widehat{\mathbf{A}_u}_\gamma \right) \right\|_2^2,$$

where the subscript $\gamma \in \{\text{steady}, \text{unsteady}\}$ denotes the corresponding subset of POD modes and coefficients. This weighting embeds a physics-informed constraint into the learning process by emphasizing the reconstruction of modes with higher energy content. Finally, the instantaneous velocity field is reconstructed by combining the estimated POD coefficients with the POD spatial modes computed from the training dataset.

The model is trained using $N_{\text{train}} = 150$ snapshots per AoA, resulting in a training sequence of approximately 0.16 s. This corresponds to about $8 - 16$ vortex shedding cycles, as defined from the shedding frequencies, and has been shown to be sufficient in Bucquet *et al.* (2025). All tests are performed on the same testing dataset consisting in $N_{\text{test}} = 50$ samples per AoA, which are not seen during training.

RESULTS

This section evaluates the performance of the SNN-POD model on both seen and unseen flow configurations. Seen configurations correspond to the angles of attack and freestream turbulence intensities on which the model was trained, while unseen (or interpolated) configurations involve AoA or TI values interpolated between the training configurations. In addition to the physical metrics introduced previously, the accuracy of the reconstructed flow state is assessed using the following classical error metrics: the **normalized mean-square error** (MSE) given by $E_{test} = \frac{1}{N_{test}} \sum_{1 \le k \le N_{test}} \frac{\left\| \mathbf{u}^k - \widehat{\mathbf{u}}^k \right\|_2}{\left\| \mathbf{u}^k \right\|_2}$, and the **fluctuation error** ε_{test}, based on the fluctuating part of the velocity field u' (with respect to the average taken over the entire the training set), defined as $\varepsilon_{test} = \frac{1}{N_{test}} \sum_{1 \le k \le N_{test}} \frac{\left\| \mathbf{u}'^k - \widehat{\mathbf{u}'}^k \right\|_2}{\left\| \mathbf{u}'^k \right\|_2}$.

The results presented below focus on the configuration with AoA = 15° and TI = 0.3. This choice is justified in the discussion of Fig.7. Fig. 4 compares characteristic features of the true and reconstructed flow fields for the sampled configuration (AoA = 15°, TI = 0.3%). Instantaneous flow features appear to be in good agreement.

A statistical comparison is provided in Fig. 5 for both steady and unsteady features. Both the wake width and wake deflection angle are perfectly recovered (Fig.5(a) and (b)). The maximum transverse gradient, $\max|\frac{\partial \overline{u}}{\partial y}|$, is also well recovered in the SNN-POD reconstruction, although minor oscillations

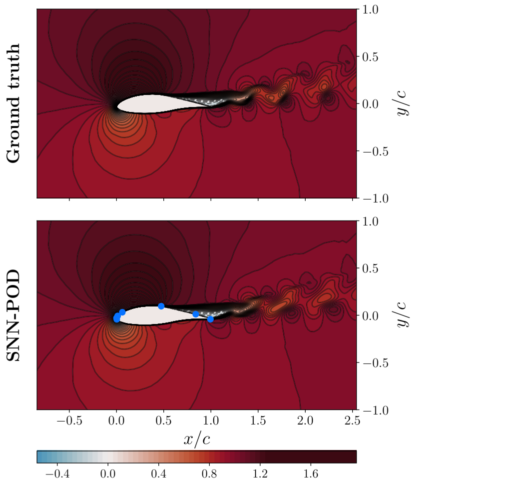

Figure 4: Comparison of streamwise velocity $u(\mathbf{x},t_s)/U_\infty$ contours at snapshot $t_s = 150$s obtained from URANS (top) and SNN-POD (bottom) for AoA= 15°, TI= 0.3%. The locations of the $p = 7$ pressure sensors on the blade, obtained with SCMV, are indicated with blue markers.

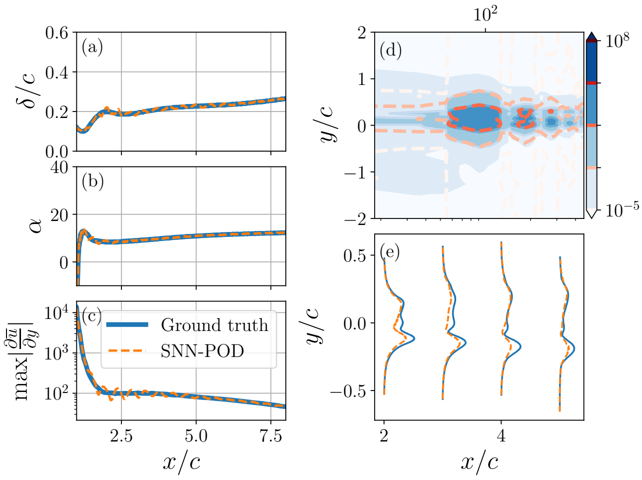

Figure 5: Comparison between the time-averaged flow features (namely, streamwise evolution of δ (a), α (b) and maximum shear (c)) and the turbulent characteristics (namely, spectrograms of fS_u in the $x/c = 2$ section (d) and vertical profiles of T_u (e)) of ground truth and reconstructed flow fields.

are observed in the near-wake region. These results hold for all tested configurations, including both sampled and interpolated cases (not shown here).

The model demonstrates consistent recovery of the turbulent metrics introduced earlier. Fig. 5(d) compares the spectrograms of the pre-multiplied time spectra of the true and estimated velocity fields in the vertical plane at $x/c = 2$. The ground truth is represented by blue shaded regions, while the reconstruction is indicated by orange dashed contours. Both use the same logarithmic colormap. The results show good accuracy, with similar energy levels and frequencies, indicating an overall good recovery of the flow's spectral content for both sampled and interpolated configurations (other configurations are not shown here). Similarly, the vertical profiles of T_u in the wake for the (AoA = 15°, TI 0.3%) case exhibit good agreement, with asymmetric profiles and peaks corresponding to the top and bottom shear layers. The bottom shear layer is the most energetic, consistent with the ground truth.

Similarly as in Fig. 2, the three time-averaged flow metrics are computed on the SNN-POD reconstructed flows from the testing dataset, and shown in Fig. 6. The near-wake profiles of the three quantities show an excellent agreement with the reference simulations, and despite some small oscillations in the maximum transverse gradient, the far-wake trends are also well recovered. Indeed, the influence of AoA and the distinction between low and moderate TI remain visible on the profiles, which indicates that the model is able to account for these two parameters.

The mean and fluctuation errors are computed individually for each sampled and interpolated configuration of the testing dataset and shown in Fig.7. The configuration (15°,0.3%), which was shown in Figs. 4-5, is associated with errors among the highest observed for the sampled configurations. This indicates that the conclusions drawn from this case remain valid for other sampled configurations. As expected, errors are higher for the interpolated configuration than for the sampled ones. Nonetheless, the mean reconstruction error remains below 4.6% (maximum observed for 15.5°), while the largest fluctuation errors $\varepsilon_{\text{test}}$ are about 42% for 15.5°.

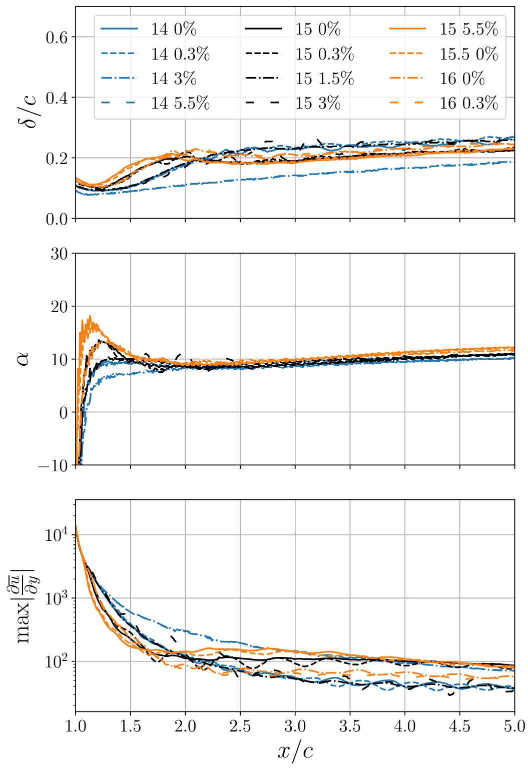

Figure 6: Streamwise evolutions of δ/c (top), α (middle) and max$|\frac{\partial \overline{u}}{\partial y}|$ (bottom) of the SNN-POD reconstructions.

CONCLUSION

The study presents a model that provides a nonlinear mapping between sparse wall pressure data and the full velocity field around the airfoil for a range of angles of attack and freestream turbulence intensities. The proposed approach integrates shallow neural networks with Reduced-Order Modeling (computed with POD) to enable efficient and low-cost flow reconstruction. A modal-splitting technique is employed to sep-

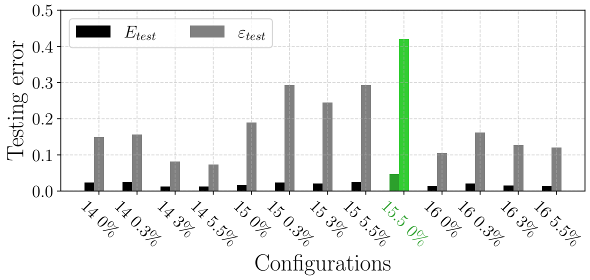

Figure 7: Testing mean error E_{test} and fluctuating error ε_{test} on testing datasets for each flow configuration. The interpolated configuration $\{15.5°, 0\%\}$ is highlighted in green.

arately handle steady and unsteady POD modes, which emerge from the multi-configuration dataset. The sensor locations are selected using a variance-based criterion.

Across all sampled and interpolated configurations, the model demonstrates a robust capability to accurately reconstruct the instantaneous streamwise velocity field, achieving a maximum reconstruction error of 5% using only a single-time set of wall pressure measurements, without requiring temporal history. Beyond classical global error metrics, the quality of the reconstruction is further assessed through a comparison of mean and turbulent local flow characteristics, in particular in the wake. In all cases, the model effectively reproduces the influence of both the angle of attack and turbulence intensity, thus demonstrating a good expressivity despite its simple architecture. The ability of the model to disentangle AoA and TI effects in the reconstructions highlights its potential for practical applications.

In future work, we plan to carry out additional studies to assess and possibly increase the suitability of the model for a real-life environment. As a first step, model interpolation abilities, which have so far only established for the angle of attack, will be tested for turbulence intensity levels, as well as for a combination of both parameters. In a second step, the model will be tested for a wider range of configurations including higher freestream turbulence levels. Finally, the approach will be extended to complex three-dimensional flow fields, including additional noise and spanwise effects. This will allow assessment of the model generalization properties and its applicability to realistic operating conditions.

REFERENCES

Braud, C., Podvin, B. & Deparday, J. 2024 Study of the wall pressure variations on the stall inception of a thick cambered profile at high Reynolds number. *Physical Review Fluids* **9** (1), 014605.

Bucquet, Q., Podvin, B., Braud, C. & Guilmineau, E. 2025 Sparse surface pressure-based reconstruction of the flow around a thick airfoil over a range of angles of attack. *(to appear in Data-Centric Engineering)* .

Devinant, P., Laverne T. Hureau J. 2002 Experimental study of wind-turbine airfoil aerodynamics in high turbulence. *J. Wind Eng. Ind. Aerod.* **90** (6), 689–707.

Erichson, N. B., Mathelin, L., Yao, Z., Brunton, S. L., Mahoney, M. W. & Kutz, J. N. 2020 Shallow Neural Networks for Fluid Flow Reconstruction with Limited Sensors. *Proceedings of the Royal Society A: Mathematical, Physical and Engineering Sciences* **476** (2238), 20200097.

Gambuzza, S. & Ganapathisubramani, B. 2023 The influence of free stream turbulence on the development of a wind turbine wake. *Journal of Fluid Mechanics* **963**, A19.

Hodgson, E. L, Madsen, M. H Aa & Andersen, S. J 2023 Effects of turbulent inflow time scales on wind turbine wake behavior and recovery. *Physics of Fluids* **35** (9).

Kaimal, J. C. & Finnigan, J. J 1994 *Atmospheric boundary layer flows: their structure and measurement*. Oxford university press.

Li, L. & Hearst, R. J. 2021 The influence of freestream turbulence on the temporal pressure distribution and lift of an airfoil. *Journal of Wind Engineering and Industrial Aerodynamics* **209**, 104456.

Maldonado, V., Castillo L. Thormann A. Meneveau C. 2015 The role of free stream turbulence with large integral scale on the aerodynamic performance of an experimental low reynolds number s809 wind turbine blade. *J. Wind Eng. Ind. Aerod.* **142**, 246–257.

Mishra, R., Guilmineau, E., Neunaber, I. & Braud, C. 2024 Developing a digital twin framework for wind tunnel testing: validation of turbulent inflow and airfoil load applications. *Wind Energy Science* **9** (1), 235–252.

Mishra, R., Neunaber, I., Guilmineau, E. & Braud, C. 2022 Wind tunnel study: is turbulent intensity a good candidate to help in bypassing low reynolds number effects on 2d blade sections? In *Journal of Physics: Conference Series*, , vol. 2265, p. 022095. IOP Publishing.

Neunaber, I., Danbon, F., Soulier, A., Voisin, D., Guilmineau, E., Delpech, P., Courtine, S., Taymans, C. & Braud, C. 2022 Wind tunnel study on natural instability of the normal force on a full-scale wind turbine blade section at Reynolds number 4.7 · 106. *Wind Energy* **25** (8), 1332–1342.

Pagamonci, L., Papi, F., Cojocaru, G., Belloli, M. & Bianchini, A. 2025 How does turbulence affect wake development in floating wind turbines? some insights from comparative large-eddy simulations and wind tunnel experiments. *Wind Energy Science* **10** (8), 1707–1736.

Porté-Agel, F., Bastankhah M. Shamsoddin S. 2020 Wind-turbine and wind-farm flows: A review. *Boundary-Layer Meteorol* **174**, 1–59.

Sheidani, A., Salavatidezfouli, S., Stabile, G. & Rozza, G. 2023 Assessment of urans and les methods in predicting wake shed behind a vertical axis wind turbine. *Journal of Wind Engineering and Industrial Aerodynamics* **232**, 105285.

Stack, J. 1931 Test in the variable density wind tunnel to investigate the effects of scale and turbulence on airfoil characteristics. *Tech. Rep.*.

Vahidi, D. & Porté-Agel, F. 2024 Influence of incoming turbulent scales on the wind turbine wake: A large-eddy simulation study. *Physics of Fluids* **36** (9), 095177.

Visonneau, M., Queutey, P., Deng, G.B., Guilmineau, E., Leroyer, A. & Wackers, J. 2014 Logiciel de simulation ISIS-CFD, version 3.0-1.